

# Revealing Active Sites and Reaction Pathways in Methane Non-Oxidative Coupling over Iron-Containing Zeolites

Hao Zhang, Aleksei Bolshakov, Raghavendra Meena, Gustavo A. Garcia, A. Iulian Dugulan, Alexander Parastaev, Guanna Li, Emiel J. M. Hensen,\* and Nikolay Kosinov\*

**Abstract:** Non-oxidative coupling of methane is a promising route to obtain ethylene directly from natural gas. We synthesized siliceous [Fe]zeolites with MFI and CHA topologies and found that they display high selectivity (>90 % for MFI and >99 % for CHA) to ethylene and ethane among gas-phase products. Deactivated [Fe]zeolites can be regenerated by burning coke in air. In situ X-ray absorption spectroscopy demonstrates that the isolated  $\text{Fe}^{3+}$  centers in zeolite framework of fresh catalysts are reduced during the reaction to the active sites, including  $\text{Fe}^{2+}$  species and Fe (oxy)carbides dispersed in zeolite pores. Photoelectron photoion coincidence spectroscopy results show that methyl radicals are the reaction intermediates formed upon methane activation. Ethane is formed by methyl radical coupling, followed by its dehydrogenation to ethylene. Based on the observation of intermediates including allene, vinylacetylene, 1,3-butadiene, 2-butyne, and cyclopentadiene over [Fe]MFI, a reaction network is proposed leading to polyaromatic species. Such reaction intermediates are not observed over the small-pore [Fe]CHA, where ethylene and ethane are the only gas-phase products.

(OCM) has been widely investigated and suffers from the low selectivity to  $\text{C}_2$  hydrocarbons due to the overoxidation towards undesired products.<sup>[1a,3]</sup> Non-oxidative methane dehydroaromatization (MDA) to aromatic products has been investigated since the 1990s.<sup>[1a,4]</sup> The main challenge relates to the rapid coking deactivation and the limited activity of typical MDA catalysts such as Mo/ZSM-5.<sup>[5]</sup> The research into non-oxidative conversion of methane was reinvigorated by the breakthrough of the Bao group in 2014 that a single-atom  $\text{Fe}@\text{SiO}_2$  catalyst displayed high activity and stability in non-oxidative coupling of methane (NOCM) to  $\text{C}_2$ -products.<sup>[3,6]</sup> The isolated nature of Fe hinders C–C coupling reactions, greatly reducing coke formation on the catalyst surface. The high selectivity towards low-value naphthalene (~25 %) remains a significant disadvantage of this catalyst.

Zeolites are crystalline microporous aluminosilicates, which can stabilize isolated metal sites in their framework or in extra-framework positions. Isomorphous substitution of Si for Fe in MFI and CHA zeolites has been studied for a variety of reactions.<sup>[7]</sup> The microporous nature of zeolites provides a confined environment, which can steer reactions, for instance, by limiting the growth of certain products.<sup>[8]</sup> In this way the formation of unwanted naphthalene product during non-oxidative conversion of methane can be suppressed. The shape-selective nature of zeolites can also be used to enhance the selectivity to specific hydrocarbons. There is a limited amount of prior work on NOCM using zeolites. Shen et al. reported a Mo/[B]ZSM-5 catalyst that reached ~90 %  $\text{C}_2\text{H}_4$  selectivity at 650 °C at a methane conversion level of 0.8 %.<sup>[9]</sup> The decreased acidity obtained by replacing Al by B was thought to contribute to a decreased formation of aro-

## Introduction

Direct upgrading of methane into value-added products is an important technology to the chemical industry.<sup>[1]</sup> One can broadly distinguish the oxidative and non-oxidative methane conversion.<sup>[2]</sup> Oxidative coupling of methane

[\*] H. Zhang, A. Bolshakov, A. Parastaev, E. J. M. Hensen, N. Kosinov  
 Laboratory of Inorganic Materials and Catalysis, Department of Chemical Engineering and Chemistry, Eindhoven University of Technology  
 5600 MB Eindhoven (The Netherlands)  
 E-mail: [e.j.m.hensen@tue.nl](mailto:e.j.m.hensen@tue.nl)  
[n.a.kosinov@tue.nl](mailto:n.a.kosinov@tue.nl)

R. Meena, G. Li  
 Biobased Chemistry and Technology, Wageningen University & Research  
 Bornse Weilanden 9, 6708 WG Wageningen (The Netherlands)  
 and  
 Laboratory of Organic Chemistry, Wageningen University & Research  
 Stippeneng 4, 6708 WE Wageningen (The Netherlands)

G. A. Garcia  
 Synchrotron SOLEIL  
 L'Orme des Merisiers, St. Aubin BP 48, 91192 Gif sur Yvette (France)

A. I. Dugulan  
 Fundamental Aspects of Materials and Energy, Department of Radiation Science and Technology, Delft University of Technology  
 Mekelweg 15, 2629 JB Delft (The Netherlands)

© 2023 The Authors. *Angewandte Chemie International Edition* published by Wiley-VCH GmbH. This is an open access article under the terms of the Creative Commons Attribution License, which permits use, distribution and reproduction in any medium, provided the original work is properly cited.

matics. Gerceker et al. evaluated a series of PtSn/ZSM-5 catalysts at 700 °C.<sup>[10]</sup> The best catalyst showed a methane conversion of 0.06 % at a C<sub>2</sub> selectivity above 90 %. Xiao et al. studied the NOCM activity of PtBi/ZSM-5 by varying the Pt/Bi ratios.<sup>[11]</sup> The authors contended that surface Pt species served as the active sites for methane activation, while Bi promoted C<sub>2</sub>-product formation. A methane conversion of 2 % was achieved from a 10 vol.% methane feed. The majority of prior work employed the ZSM-5 zeolite. Compared to this 10-membered ring (10MR) zeolite, the smaller pore windows in the 8MR CHA zeolite can further enhance the selectivity towards light hydrocarbon products.<sup>[12]</sup>

There remains a significant lack of understanding of the reactive chemistry during zeolite-catalyzed methane conversion, pertaining mostly to the nature of the active sites, the reaction mechanism and the contribution of gas-phase reactions. Several in situ characterization techniques have already been deployed to resolve these matters.<sup>[13]</sup> Chen et al. used in situ X-ray absorption spectroscopy (XAS) and in situ X-ray diffraction (XRD) to investigate the structure of Pt–Bi/ZSM-5 catalysts used in the NOCM reaction and reveal the formation of an intermetallic surface Pt<sub>3</sub>Bi phase on top of a Pt core.<sup>[14]</sup> Using online vacuum ultraviolet soft photoionization molecular-beam mass spectrometry, Bao and co-workers proposed the formation of methyl radicals during methane conversion over isolated Fe centers in Fe@SiO<sub>2</sub>.<sup>[6]</sup> Photoelectron photoion coincidence spectroscopy (PEPICO) is a related tool which combines photoelectron spectroscopy (PES) with soft photoionization mass spectrometry to improve the analysis of different isomers.<sup>[15]</sup> The group of van Bokhoven used this technique to study the gas-phase intermediates formed over Fe/SiO<sub>2</sub> catalyst. In addition to the methyl radicals observed by Bao and co-workers,<sup>[6]</sup> they found that propargyl radicals (H<sub>2</sub>C–C≡C–H<sup>•</sup>) are likely precursors to aromatic products.<sup>[16]</sup>

Herein, we aimed at improving the C<sub>2</sub> selectivity of the Fe-catalyzed NOCM reaction by using the effect of zeolite confinement. Specifically, we synthesized a series of Al-free shape-selective siliceous zeolites with CHA (8MR) and MFI (10MR) structures in which Fe was the sole substituent for Si. Combining various characterization techniques, we could follow the evolution of the structure of Fe species during the catalyst life and make proposals for the NOCM reaction pathway over these catalysts.

## Results and Discussion

[Fe]CHA and [Fe]MFI zeolites were obtained by specifically developed direct hydrothermal synthesis techniques. The actual Si/Fe ratios were close to the intended values (Table S1). The particle size of fresh catalysts ranges from 0.5 to 1.5 μm, as shown in the scanning electron microscopy (SEM) images (Figure S1 and Table S1). Ar physisorption isotherms demonstrate that the catalysts are microporous zeolites (Table S1 and Figure S2). The synchrotron XRD patterns of the directly synthesized FeCHA100 and FeM-

FI100 (here “100” denotes the Si/Fe atomic ratio) and the reference samples, prepared by impregnation with iron nitrate and calcination, confirm the presence of zeolites with the CHA and MFI topologies, respectively (Figure 1a). The diffraction peak at ~2.5 Å<sup>-1</sup> in the patterns of FeMFI100-imp and FeCHA100-imp catalysts can be ascribed to the Fe<sub>2</sub>O<sub>3</sub> phase (PDF no. 00-039-1346). The Fourier-transformed extended X-ray absorption fine structure (FT-EXAFS) at the Fe K-edge features one coordination shell originating from the Fe–O single scattering path, demonstrating the presence of isolated Fe sites in Fe-CHA100 and FeMFI100 catalysts (Figure 1b). The FT-EXAFS spectra of the impregnated samples have similar features as the bulk Fe<sub>2</sub>O<sub>3</sub> reference (Figure 1b). The XRD and EXAFS data obtained for the directly synthesized [Fe]zeolite samples with Si/Fe ratios of 200 and 80 also support the conclusion that the samples predominantly contain isolated Fe species (Figure S3, S6, S7, and Table S2). The presence of isolated Fe centers was further confirmed by the wavelet transformed (WT) EXAFS, in which only one major WT maximum can be seen at ~7 Å<sup>-1</sup> (Figure S4), whereas an additional WT maximum (7.5 Å<sup>-1</sup>, 2.7 Å) is present in the spectra of impregnated catalysts, indicative of the presence of Fe<sub>2</sub>O<sub>3</sub> (Figure S5).

The results of  $K\beta_{1,3}$  X-ray emission spectroscopy (XES) and Fe 2p X-ray photoelectron spectroscopy (XPS) analysis show that iron is present as Fe<sup>3+</sup> in fresh samples (Figures S8, S9). High energy resolution fluorescence detected X-ray absorption near edge structure (HERFD-XANES) is one of the most suitable technique to study the pre-edge features corresponding to the 1s to 3d electronic transitions and reflecting the oxidation state and coordination geometry of Fe-centers (Figure 1c, Figure S10).<sup>[17]</sup> The pre-edge peak area and pre-edge centroid of [Fe]zeolite catalysts for the FeCHA100 and FeMFI100 catalysts are close to the FePO<sub>4</sub> reference with tetrahedral coordination (Fe<sup>3+</sup> Td). On the contrary, the results for the impregnated catalysts (FeCHA100-imp and FeMFI100-imp) are close to the FePO<sub>4</sub>·2H<sub>2</sub>O reference, where Fe is in octahedral coordination (Fe<sup>3+</sup> Oh) (Figure S11, S12, and Figure 1d). These findings indicate the presence of mainly Fe<sup>3+</sup> Td sites in the directly synthesized [Fe]zeolite catalysts, whereas the impregnated catalysts contain mainly Fe<sup>3+</sup> Oh centers like Fe<sub>2</sub>O<sub>3</sub>, in line with the valence-to-core XES results (Figure S13).<sup>[17]</sup>

The aggregation extent and coordination state of Fe<sup>3+</sup> were confirmed by Ultraviolet-Visible diffuse reflectance spectroscopy (UV/Vis DRS, Figure 1e). The isolated tetrahedral Fe<sup>3+</sup> sites display two oxygen-to-metal charge transfer (CT) bands at ~211 and ~245 nm, while the feature at ~277 nm can be attributed to isolated octahedral Fe<sup>3+</sup>.<sup>[18]</sup> The CT bands located at ~333 nm and ~427 nm are ascribed to oligomeric Fe<sup>3+</sup> clusters and larger Fe<sub>2</sub>O<sub>3</sub> aggregates, respectively.<sup>[18]</sup> Compared with the directly synthesized [Fe]zeolite catalysts, the impregnated references show pronounced features at wavenumbers higher than 300 nm, suggesting the existence of larger Fe clusters and even Fe<sub>2</sub>O<sub>3</sub> particles. UV/Vis DR spectra of the directly synthesized catalysts were deconvoluted using 5 compo-

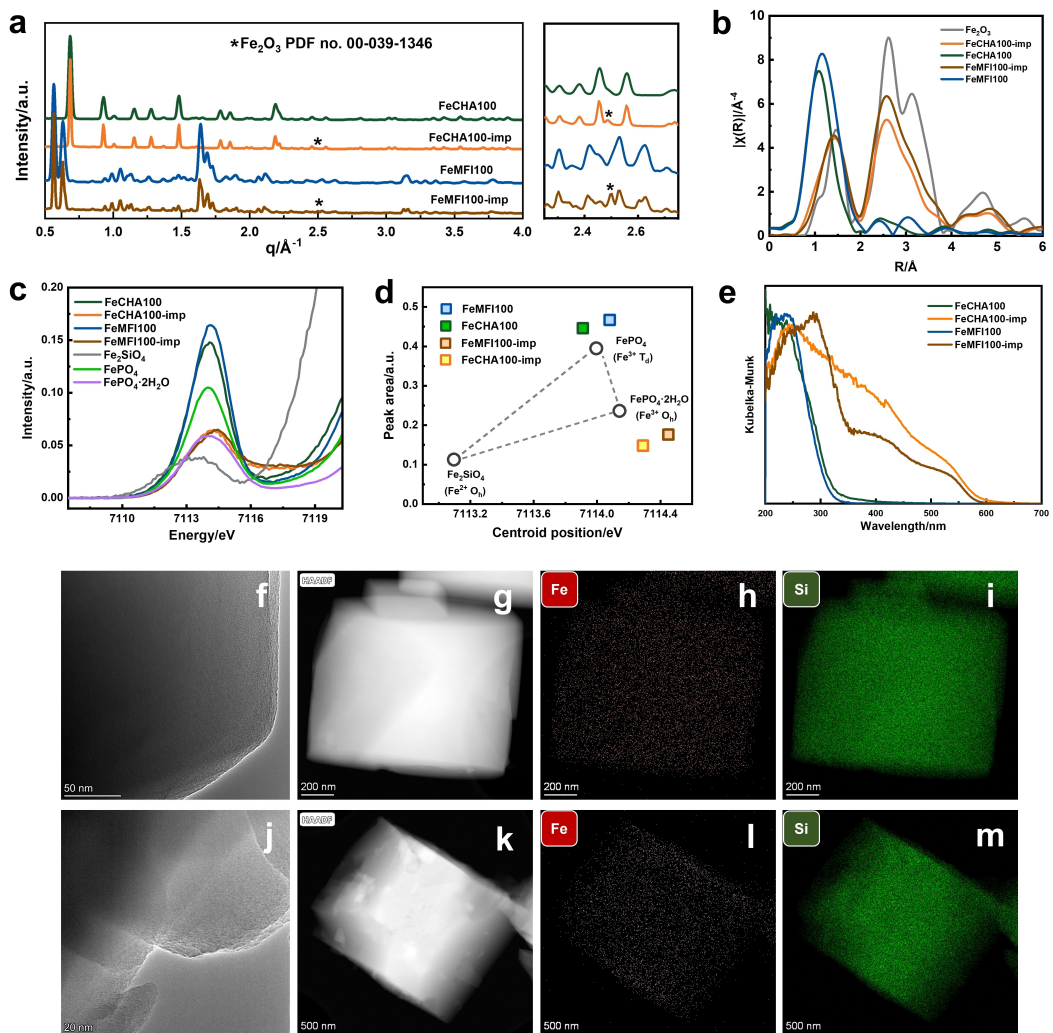


**Figure 1.** (a) Synchrotron XRD patterns, (b)  $k^3$ -weighted Fourier transformed Fe K-edge EXAFS, (c) Pre-edge region of HERFD-XANES, and (d) the related pre-edge peak analysis. (e) UV/Vis DRS of fresh Fe/zeolite catalysts. (f) AC-TEM image, (g) High-angle annular dark-field scanning transmission electron microscopy (HAADF-STEM) image, and (h,i) the corresponding STEM-EDX results of the fresh FeMFI100. (j) AC-TEM image, (k) HAADF-STEM image, and (l,m) the corresponding STEM-EDX results of the fresh FeCHA100 catalyst.

ments, as shown in Figure S14 and S15.<sup>[18]</sup> The results indicate that the fresh samples also contain isolated Fe<sup>3+</sup> *Oh* and Fe aggregates. The Fe *Td* species represent Fe cations isomorphously substituted in the zeolite framework, while the Fe *Oh* species are located outside the framework.<sup>[19]</sup> The presence of Fe species in the zeolite framework is further confirmed by Raman spectra (Figure S16). A comparison with simulated XANES of the density functional theory (DFT)-optimized framework Fe model also indicates that the majority of Fe is in the framework (Figure S17). Besides, transmission electron microscopy (TEM) and scanning transmission electron microscopy-energy dispersive X-ray spectroscopy (STEM-EDX) analysis of one-step synthesized catalysts support the highly dispersed state of Fe (Figure 1f-m, Figure S18 to S20). To summarize, one-step synthesized [Fe]zeolite catalysts mainly contain isolated tetrahedral coordinated Fe<sup>3+</sup> species in the zeolite framework, together with a small minority of Fe<sup>3+</sup> *Oh* species and Fe aggregates located at

extra-framework positions. Fe<sub>2</sub>O<sub>3</sub> nanoparticles and Fe-oxo clusters were the main Fe-species in the impregnated catalysts.

The catalytic performance of Fe/zeolite catalysts and siliceous MFI and CHA zeolites in NOCM reaction at 750°C is shown in Figure 2a. The Fe-containing zeolites displayed a substantially higher activity than the siliceous Fe-free CHA and MFI samples. From the observation that the activity increased with Fe content, it can be derived that Fe plays a catalytic role. The one-step synthesized [Fe]zeolite catalysts perform much better than their impregnated counterparts with similar Fe loading. While ethane and ethylene were the only detected gas-phase products over the Fe/CHA catalysts, Fe/MFI also led to the formation of benzene and toluene. The formation of larger reaction products in the [Fe]MFI samples can be explained by the larger pores in this zeolite, whereas bulky aromatic molecules cannot leave the small pores of CHA zeolites. Naphthalene was not observed by gas chromatography-

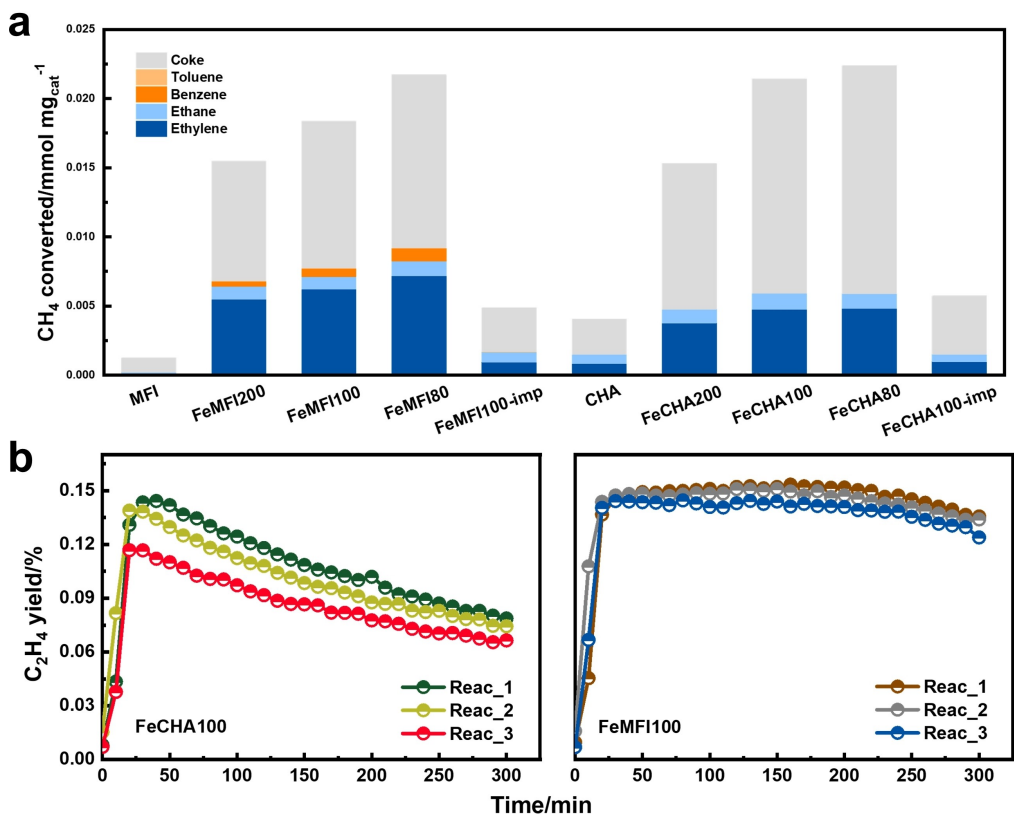


**Figure 2.** (a) Catalytic performance of the various catalyst samples at a pressure of 1 bar. (b) Reaction-regeneration tests of FeCHA100 and FeMFI100 (750 °C; 20 mL/min 95 vol.% CH<sub>4</sub> and 5 vol.% Ar; 50 mg catalyst). Catalyst regeneration carried out at 650 °C for 1 h in air. In Reac\_x, x refers to the reaction cycles upon intermittent regeneration.

flame ionization detection (GC-FID) analysis of the product stream in any of the experiments. The much higher specific surface area and pore volume of CHA results in more interactions between CH<sub>4</sub> and the hot zeolite surface (Table S1). This can explain why CHA shows a higher C<sub>2</sub>-hydrocarbon yield than MFI. The long-term activity tests in the NOCM reaction, performed at different temperatures over FeCHA100 and FeMFI100 catalysts, are shown in Figure S21. With the increase of reaction temperature from 700 to 800 °C, the initial ethylene yield increased from ~0.05 % to ~0.25 % for both catalysts, although shortening the catalyst lifetime. Catalyst deactivation is likely due to the formation of coke, which blocks the zeolite pores. Variation of the reaction pressure showed that the cumulative C<sub>2</sub> hydrocarbon yield can be significantly increased ( $\approx$ 3 times) by increasing methane partial pressure from 0.5 to 5 bar (Figure S22). This can be ascribed to the reversible nature of coke formation. Coke hydrogenation is facilitated at higher reaction pressures, reducing the negative impact of coke deposits in the micropores on the activity.<sup>[20]</sup> Figure 2b shows results of reaction-regeneration tests performed with FeCHA100 and FeMFI100 catalysts. Catalyst deactivation is evident for both catalysts in terms of decreasing ethylene yield. The methane conversion decreased from ~2 % to ~0.5 % during the 5 h NOCM reaction for FeCHA100 and FeMFI100 catalysts (Figure S23). Due to the smaller pore windows in [Fe]CHA,

aromatics formed inside zeolite pores cannot escape compared with [Fe]MFI catalysts, which led to faster deactivation profiles (Figure 2b). This can explain the stronger deactivation observed for FeCHA100. The [Fe]zeolite catalysts exhibit enhanced catalytic performance in terms of reaction rate compared with reported zeolite-based catalysts in NOCM reaction (Table S3).

We performed aberration corrected (AC)-TEM and STEM-EDX to investigate the [Fe]zeolite catalysts after the NOCM reaction. The majority of Fe species remain highly dispersed, although some Fe particles with a size larger than 10 nm can be found (Figure 3a–f, Figure S24 to S27). These Fe particles, located on the external surface of zeolites, were not observed in fresh catalysts. Quasi in situ Mössbauer spectroscopy demonstrated the presence of three types of Fe species, namely metallic Fe, Fe (oxy)carbide, and Fe<sup>2+</sup>-centers in used catalysts (Figure 3g and Figure S28). As the Mössbauer spectra were recorded at 4.2 K, the Fe distribution can be calculated as well (Figure 3h and Table S4). For small Fe (oxy)carbide species, the Mössbauer spectrum would have been paramagnetic, appearing as a doublet.<sup>[21]</sup> This points to the very limited aggregation of Fe (oxy)carbides in the zeolite cages. At cryogenic temperatures, both catalysts display similar values of the hyperfine field related to metallic Fe species (~33.8 T, Table S4), which suggests the presence of bulk Fe<sup>0</sup> particles (~10 to 15 nm).<sup>[22]</sup> This means that the nano-

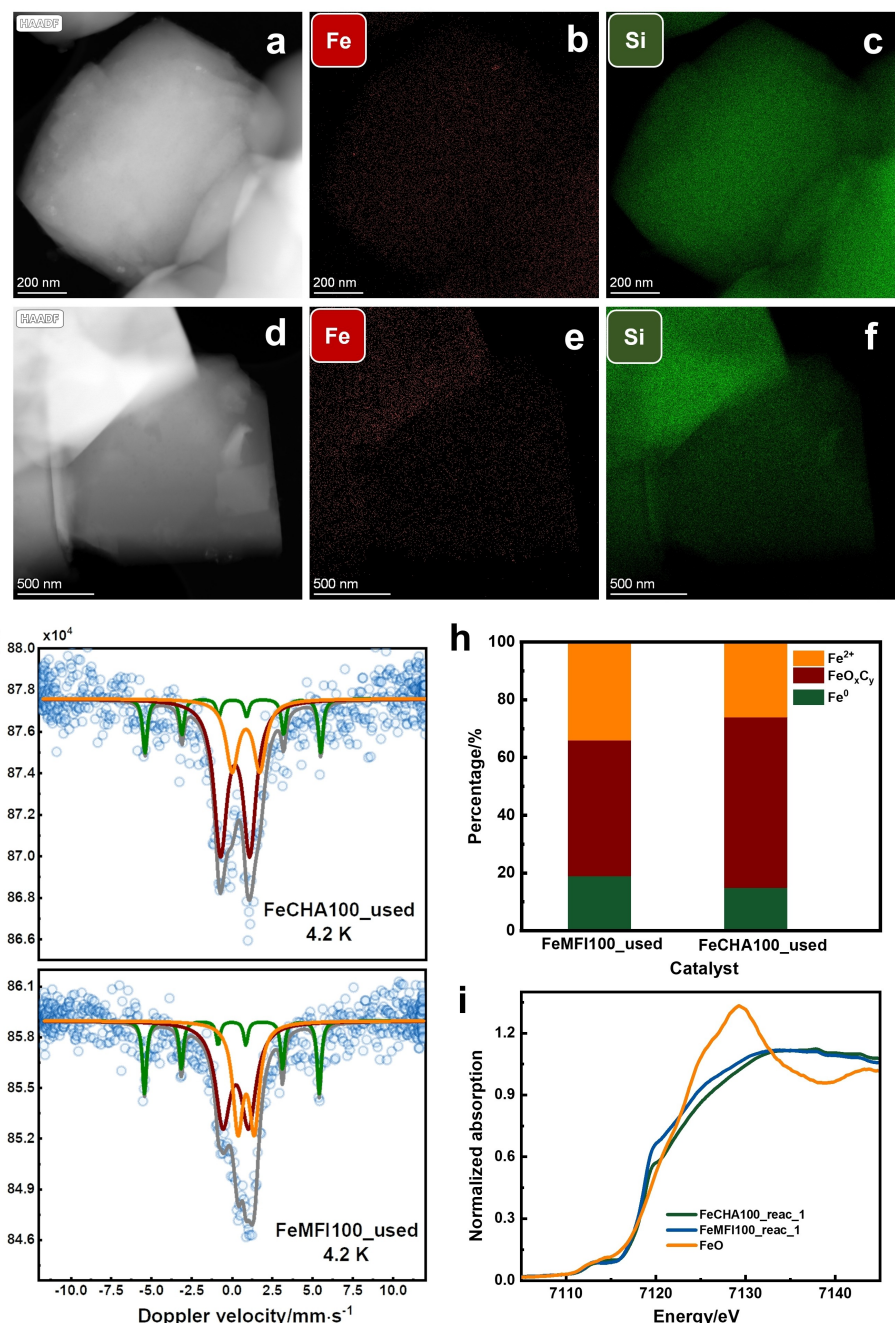


**Figure 3.** (a) HAADF-STEM and (b, c) STEM-EDX results of used FeMFI100 catalysts. (d) HAADF-STEM and (e, f) STEM-EDX analysis of used FeCHA100 catalysts. (g) Mössbauer spectra of used FeCHA100 and FeMFI100 catalysts. Grey: envelop; Green: metallic Fe; orange: Fe<sup>2+</sup>; wine: FeO<sub>x</sub>C<sub>y</sub>. (h) The percentages of FeO<sub>x</sub>C<sub>y</sub>, Fe<sup>2+</sup>, and Fe<sup>0</sup> obtained from Mössbauer analysis. (i) Normalized XANES of working [Fe]zeolite catalysts and FeO. The spectra of working catalysts were collected at the end of the first reaction runs at 750°C.

particles observed at the external zeolite surface by STEM-EDX are metallic Fe particles. The formation of bulk Fe<sup>0</sup> was furthermore confirmed by analyzing the used Fe-CHA100 at room temperature, where a sextuplet with a hyperfine field of ~33 T was observed (Figure S29 and Table S5). The resistance of a particular fraction of Fe<sup>2+</sup> species against sintering is most likely due to their anchoring to the defective zeolite framework.<sup>[23]</sup> We also analyzed the XANES spectra recorded at the end of each

reaction cycle (Figure 3i and Figure S30). Although more than half of Fe appears to be in a Fe (oxy)carbide phase in the used catalysts according to Mössbauer analysis, the position of the rising edge is close to that of FeO. This finding confirms the strong interaction between zeolite and the confined Fe (oxy)carbide species, resulting in strong stabilization of the partially oxidized Fe-species.

To investigate the structure of Fe sites during the NOCM reaction, we carried out *in situ* quick XAS

measurements in quartz capillary reactors at methane partial pressures of 1 bar, 0.5 bar and 5 bar with intermittent regeneration by calcination (Figure S31, S32). The rising edge that shifts to lower energy and the gradually decreasing pre-edge peak intensity during each reaction cycle suggest the reduction of initial Fe species and a possible change in the Fe coordination environment (Figure S33, S34). Differences can also be distinguished in the  $k$ -space and Fourier-transformed EXAFS spectra, in which the amplitude of the Fe–O/C shell varies (Figure S35, S36). The absence of a strong signal originated from the second backscatter suggests the dispersed nature of Fe throughout the whole process. We analyzed these data in more detail by linear combination fitting (LCF), pre-edge peak fitting, and EXAFS fitting (Figure 4). The presence of isosbestic points suggests that the initial framework Fe sites are transformed without intermediate to their final states (Figure S33, S34).<sup>[24]</sup> There are subtle differences among the final spectra between the reaction cycles (Figure S37). Accordingly, we used the initial and final XANES spectra in each reaction cycle as references for LCF fitting. In the first run, the FeCHA100 and FeMFI100 catalysts were not fully reduced even when the temperature reached 750 °C. However, the reduction of Fe species was more facile in the second run. Less significant differences can be observed between the third and the second runs. The shift of the pre-edge centroid to a lower energy also reflects the reduction of Fe species, and the easier Fe reduction in the second and

the third runs can be observed (Figure 4). These findings are indicative of the extraction of Fe species from zeolite framework to the zeolite cages during the successive reduction-regeneration cycles. EXAFS analysis displayed the slight decrease of the coordination number of the first shell during the NOCM reaction, which can be ascribed to the formation of Fe (oxy)carbides or Fe<sup>2+</sup> species with lower coordination number (Figure 4, Note S1 and Table S6). A possible reaction pathway for the evolution of Fe centers based on DFT calculations is given in the Supporting Information (Figure S38, S39, Note S2). The study of regenerated catalysts indicates the formation of Fe<sub>2</sub>O<sub>3</sub> aggregates after multiple reaction-regeneration cycles and irreversible changes of the zeolite framework. Acidity characterization using infrared (IR) spectroscopy of adsorbed pyridine for the [Fe]MFI catalysts indicates that Brønsted acid sites do not play a significant role in the NOCM reaction (Figure S40 to S49, Table S7 to S9, Note S3).

Based on above analysis, the fresh [Fe]zeolite catalysts mainly contain isolated Fe<sup>3+</sup> *Td* species located in zeolite framework. Quasi *in situ* Mössbauer spectra recorded after 5 h of NOCM reaction revealed a significant fraction of Fe as finely dispersed (oxy)carbides in the zeolite cages (Table S4). A smaller fraction of metallic Fe particles (< 20 %) was found at the external surface in keeping with TEM analysis. The rest of Fe (~30 %) are Fe<sup>2+</sup> species likely strongly anchored to the defective zeolite framework.

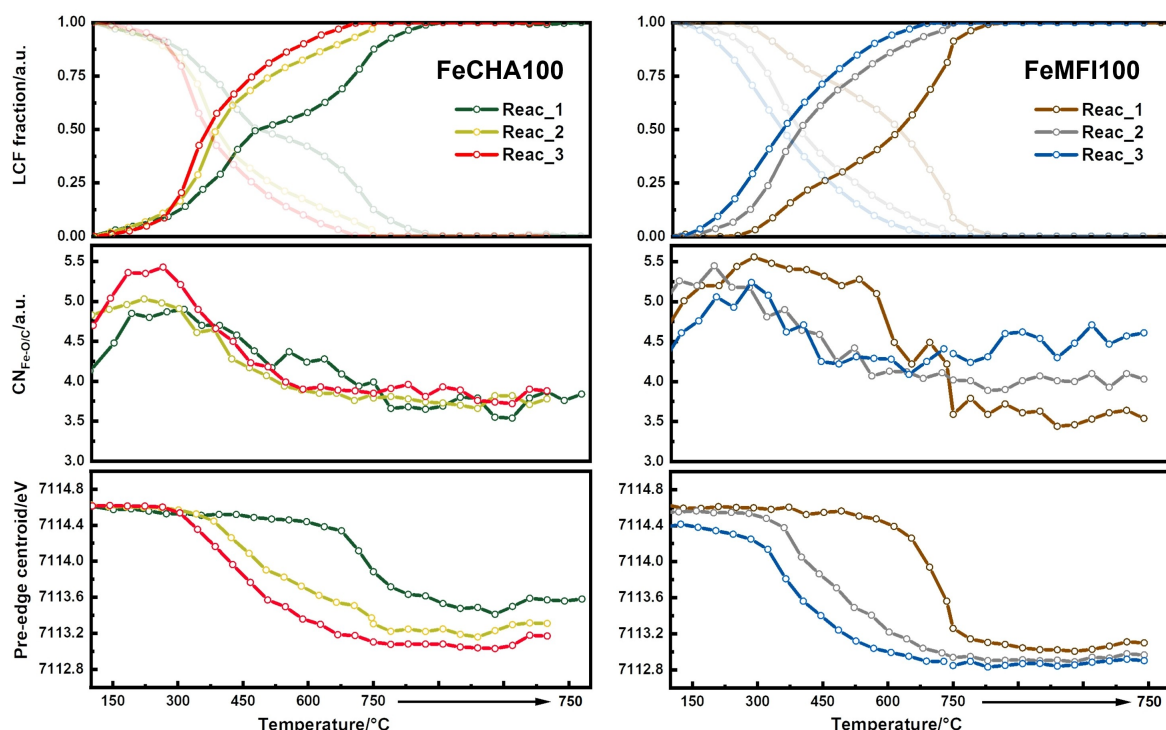


**Figure 4.** The evolution of LCF fractions (the semi-transparent lines show the evolution of components with the spectra collected before reaction), Fe–O/C coordination number, and the pre-edge centroid, obtained during *in situ* quick XAS measurements. The tests were performed from room temperature to 750 °C using a ramping rate of 10 °C/min, and hold at 750 °C for 30 min. 4 mg catalysts and 20 mL/min CH<sub>4</sub> were used.

Such  $\text{Fe}^{2+}$  sites can display some heterogeneity with different degrees of coordinative unsaturation.<sup>[23]</sup> The evolution of framework Fe was also tracked by *in situ* XAS during the reaction-regeneration cycles. Regeneration by air to remove coke led to the reoxidation of Fe-species to  $\text{Fe}^{3+}$ . Reduction of these  $\text{Fe}^{3+}$  species to  $\text{Fe}^{2+}$  during subsequent NOCM reaction runs was easier for the FeCHA100 and FeMFI100 catalysts (Figure 4). Clear features of Fe (oxy)carbides and metallic Fe are absent in the XAS analysis, which can be ascribed to their disordered structure and high dispersion. The active sites for the NOCM reaction are likely  $\text{Fe}^{2+}$  sites stabilized by the defective framework, as also supported by the DFT analysis, and highly dispersed Fe (oxy)carbides dispersed in the zeolite cages. We speculate that Fe (oxy)carbide also interacts with the defective zeolite framework possibly involving  $\text{Fe}^{2+}$  as well, which may explain the high stability against sintering under the harsh conditions applied. Metallic Fe particles do not significantly contribute to methane activation considering the low activity of the impregnated catalysts containing mainly metallic Fe (Figure 2a, S50). Moreover, in the best performing substituted zeolites the amount of metallic Fe is small as compared to  $\text{Fe}^{2+}$  and Fe (oxy)carbides. Despite the slight decrease in the ethylene yield in the second and third reaction runs (Figure 2b), the relatively stable catalytic performance during the reaction-regeneration cycles can be explained by the high stability of the Fe phases present in the zeolite pores against sintering. It is difficult to discern the catalytic role of  $\text{Fe}^{2+}$  species and Fe (oxy)carbides in the NOCM reaction. However, assuming that more Fe (oxy)carbide is formed at the expense of isolated  $\text{Fe}^{2+}$  during consecutive reaction-regeneration cycles, the increased coke amount in the second run may indicate a higher coke selectivity of Fe (oxy)carbide as compared with  $\text{Fe}^{2+}$  species (Figure S51).

To understand the underlying mechanism of the conversion of methane to products including ethylene, ethane, and (poly)aromatics, we deployed PEPICO for the Fe-CHA100 and FeMFI100 at 750 °C under 0.8 bar of methane partial pressure. This technique can help to detect short-lived intermediates, which are usually difficult to observe by conventional analytic techniques. The configuration of the PEPICO experiment is sketched in Figure S52 and more experimental details are given in the Supporting Information. The ionization energy was set at 10.2 eV, which is below the ionization energy of methane (12.6 eV) but higher than the ionization energy of methyl radical (9.8 eV).<sup>[6]</sup> This approach helps avoiding the formation of fragments with  $m/z = 15$  from ionization of unconverted  $\text{CH}_4$ . Therefore, ions with  $m/z = 15$  only correspond to methyl radicals. Due to the coincident detection of ions and electrons, the pure PES of each of the products of soft ionization seen in the time-of-flight mass spectrum (TOF-MS) can be extracted and used for unambiguous identification of the gas-phase species, including possible isomers.

Figure 5a displays the PES of  $m/z = 15$  species obtained for the FeCHA100 and FeMFI100 catalysts. The photo-electron spectra match that of the methyl radical.<sup>[25]</sup> In light

of the enhanced catalytic performance of [Fe]zeolites compared with reference samples without Fe (Figure 2a), we infer that methyl radicals are mainly formed on Fe sites, although there is also a contribution of the hot zeolite surface. Since the methyl radicals diffuse through the gas phase before detection, it is likely that the following C–C coupling reactions occur in the zeolite pores. Although only  $\text{CH}_3\cdot$  was observed over the [Fe]CHA catalyst, additional larger reaction intermediates including allene,<sup>[26]</sup> vinylacetylene,<sup>[27]</sup> 1,3-butadiene,<sup>[28]</sup> 2-butyne,<sup>[29]</sup> and cyclopentadiene<sup>[30]</sup> were detected over [Fe]MFI. The difference can be explained by the small size of the pore windows of CHA zeolites, which hinders the diffusion of larger hydrocarbon fragments out of [Fe]CHA (Figure 5a). Ethane and ethylene molecules cannot be ionized at the applied ionization energy of 10.2 eV. Moreover, we did not observe  $\text{C}_2$  intermediates including  $\text{CH}_3\text{--CH}_2\cdot$  and  $\text{CH}_2=\text{CH}\cdot$ , which can in principle be detected at 10.2 eV (Figure S53).<sup>[31]</sup> It is possible that these reaction intermediates are below the detection limit of PEPICO. We speculate that ethane is the primary  $\text{C}_2$  hydrocarbon product, which was obtained by the coupling of methyl radicals. Ethane is then likely dehydrogenated to ethylene in keeping with the ethylene formation pathway proposed by Bao and co-workers.<sup>[6]</sup> Gas-phase ethane dehydrogenation measurements further support the proposed ethylene formation process (Figure S54). Nevertheless, the role of catalytic Fe centers and the zeolite surface in the present study for ethane activation cannot be excluded under the applied conditions. Ethylene is then a precursor to the further growth into  $\text{C}_3$  to  $\text{C}_5$  hydrocarbons, aromatics, and deactivating polycyclic aromatic species as shown in Figure 5b.

Complementary to the light hydrocarbon intermediates observed by PEPICO, we performed *in situ* Raman over FeCHA100 and FeMFI100 catalysts to study the evolution of heavy hydrocarbon components retained inside the zeolite pores. The *in situ* Raman spectra were obtained simultaneously with the *in situ* quick XAS presented above. The resulting Raman spectra contain similar features for the FeCHA100 and FeMFI100 catalysts, indicating the generation of the same confined hydrocarbon species in both samples (Figure S55). For identification of the Raman features, we employed the assignments in Table S10. Peak fitting was based on these assignments (Figure S56). The Raman signal of hydrocarbon species can already be detected before reaching the reaction temperature of 750 °C, implying that the reaction already starts before Fe is fully reduced (Figure 4). The signal belonging to phenanthrene or methylated benzenes increased and then levelled off during the NOCM reaction at 750 °C and 1 bar. On the contrary, the signal assigned to either conjugated olefins or cyclopentadienyl species decreased, suggesting that there is a dehydrogenation pathway of these species to aromatics. Furthermore, the evolution of these hydrocarbon species was affected by the reaction pressure. While these hydrocarbon components evolved slower at 0.5 bar, this process was much faster during the reaction at 5 bar (Figure S56). The following evolution of confined hydrocarbons towards coke was investigated by operando time-

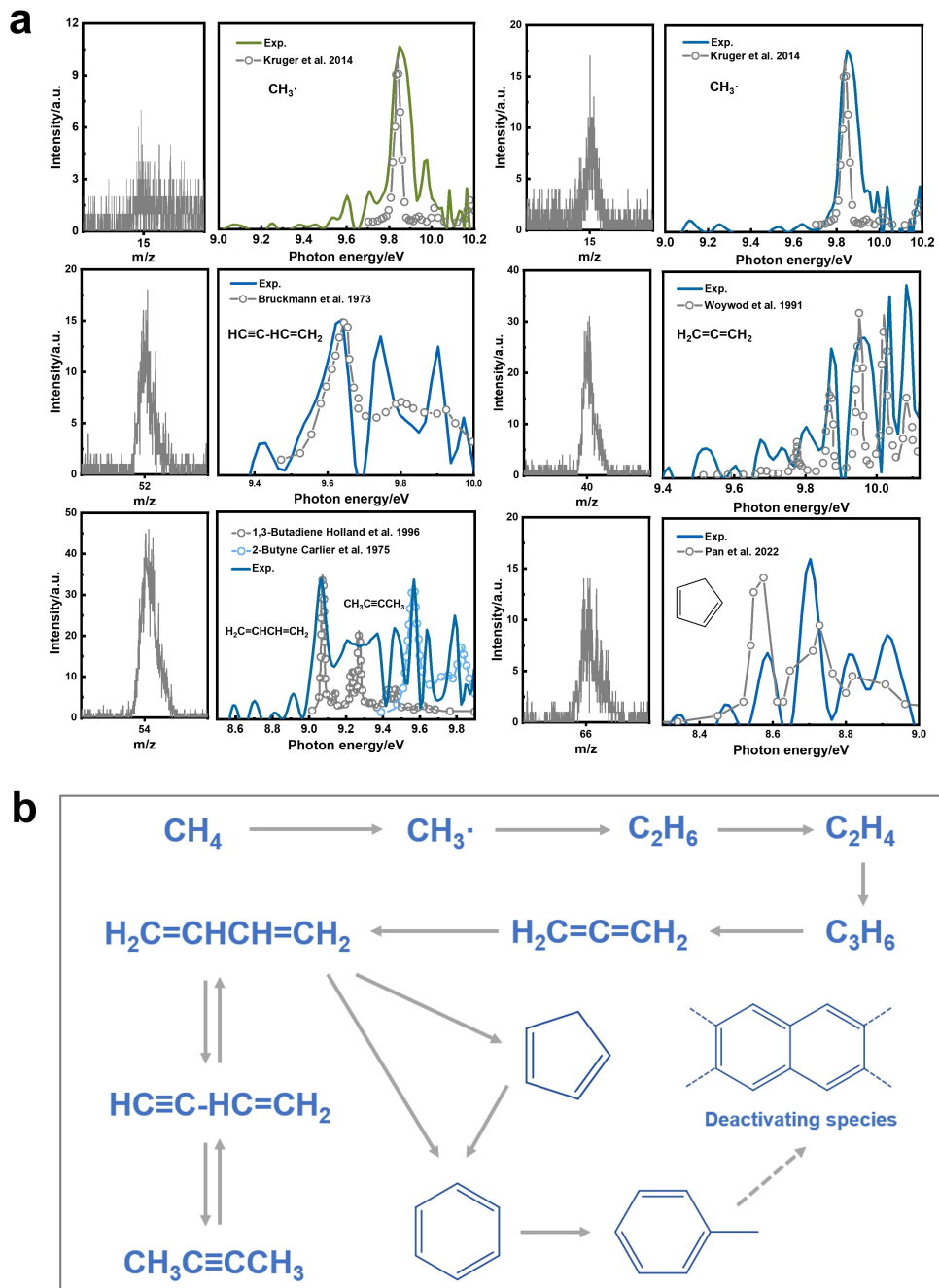


**Figure 5.** (a) TOF-MS and the corresponding PES of gas-phase intermediates obtained from PEPICO at 750 °C. The intermediate detected over FeCHA100 is shown using the green line and the intermediate species diffused from FeMFI100 are shown using blue lines. (b) A possible reaction network governing the conversion of methane over [Fe]zeolite catalysts.

resolved synchrotron XRD (Figure S57 to S59, Note S4). The gradual build-up of coke from the inlet to the outlet of the reactor was tracked by the expansion of zeolite unit cell, indicating the progressive deactivation along the catalyst bed.

## Conclusion

To summarize, a comparison of isomorphously substituted [Fe]CHA and [Fe]MFI with impregnated Fe/CHA and Fe/MFI counterparts demonstrates the enhanced performance when starting from the high (framework) Fe dispersion in the former samples. The [Fe]zeolite catalysts exhibit relatively stable performance in three reaction-regeneration cycles. [Fe]MFI catalysts display a  $\text{C}_2$  selectivity of >90 % with benzene and toluene as the main gas-phase

side-products, while the C<sub>2</sub> selectivity over [Fe]CHA catalysts is >99 %. The initial framework Fe<sup>3+</sup> species are reduced to the active sites, which include Fe<sup>2+</sup> species and Fe (oxy)carbides stabilized by the defective zeolite framework, during the reaction. The proposed mechanism involves the formation of gas-phase methyl radicals through direct methane activation on Fe centers, which yields ethane by C–C coupling followed by dehydrogenation to ethylene. The reaction network also features formation of C<sub>3</sub> to C<sub>5</sub> species including allene, vinyl-acetylene, 1,3-butadiene, 2-butyne, cyclopentadiene, which are eventually transformed into polyaromatic deactivating species.

### Acknowledgements

The work is support by the Advanced Research Center for Chemical Building Blocks that co-founded and co-financed by the Netherlands Organization for Scientific Research (NWO) and the Netherlands Ministry of Economic Affairs. We acknowledge the European Synchrotron Radiation Facility for provision of synchrotron radiation facilities and we thank Jacob Drnec and Veijo Honkimäki for assistance in using beamline ID31 under the proposal no. MA4586. We acknowledge Blanka Detlefs for the help in using beamline ID26 under the proposal no. MA5121. We acknowledge SOLEIL for provision of synchrotron radiation facilities related to the experiments at beamline DESIRS and ROCK under project no. 20200257 and 20210495, respectively. We acknowledge Laurent Nahon, Stephanie Belin, and Valerie Briois for the assistance. The experiments performed at ROCK were supported by a public grant overseen by the French National Research Agency (ANR) as part of the “Investissements d’Avenir” program (reference: ANR-10-EQPX-45). The DFT calculations were performed using the Dutch national e-infrastructure with the support of the SURF Cooperative using grant no. EINF-3542, financed by NWO. We thank Anna Litkova, Valentin Jestl, Valery Muravev, and Angelina Evtushkova for assisting with synchrotron experiments. We thank Peerapol Pornsetmetakul for the assistance with IR measurements. We acknowledge Adelheid M. Elemans-Mehring and Maarten Theelen for the assistance with inductively coupled plasma-optical emission spectroscopy analysis.

### Conflict of Interest

The authors declare no conflict of interest.

### Data Availability Statement

The data that support the findings of this study are available from the corresponding author upon reasonable request.

**Keywords:** C–C Coupling · Iron · Methane · Non-Oxidative · Zeolites

- [1] a) H. Zhang, E. J. M. Hensen, N. Kosinov, *Comprehensive Inorganic Chemistry III, Third Edition*, Vol. 6, Elsevier, Amsterdam **2023**, pp. 311–326; b) D. Kiani, S. Sourav, Y. Tang, J. Baltrusaitis, I. E. Wachs, *Chem. Soc. Rev.* **2021**, *50*, 1251–1268.
- [2] X. Huang, X. Jiao, M. Lin, L. Jia, B. Hou, D. Li, *J. Fuel Chem. Technol.* **2018**, *46*, 1087–1100.
- [3] P. Schwach, X. Pan, X. Bao, *Chem. Rev.* **2017**, *117*, 8497–8520.
- [4] O. V. Bragin, T. V. Vasina, A. V. Preobrazhenskii, K. M. Minachev, *Bull. Acad. Sci. USSR Div. Chem. Sci. (Engl. Transl.)* **1989**, *38*, 680–680.
- [5] a) L. Wang, L. Tao, M. Xie, G. Xu, J. Huang, Y. Xu, *Catal. Lett.* **1993**, *21*, 35–41; b) N. Kosinov, E. J. M. Hensen, *Nanotechnology in Catalysis*, Wiley-VCH, Weinheim **2017**, pp. 469–482.
- [6] X. Guo, G. Fang, G. Li, H. Ma, H. Fan, L. Yu, C. Ma, X. Wu, D. Deng, M. Wei, D. Tan, R. Si, S. Zhang, J. Li, L. Sun, Z. Tang, X. Pan, X. Bao, *Science* **2014**, *344*, 616–619.
- [7] a) R. Pérez Vélez, I. Ellmers, H. Huang, U. Bentrup, V. Schünemann, W. Grünert, A. Brückner, *J. Catal.* **2014**, *316*, 103–111; b) M. Yabushita, H. Kobayashi, A. Neya, M. Nakaya, S. Maki, M. Matsubara, K. Kanie, A. Muramatsu, *CrystEngComm* **2020**, *22*, 7556–7564; c) K. Niu, G. Li, J. Liu, Y. Wei, *J. Solid State Chem.* **2020**, *287*, 121330.
- [8] a) H. Wang, L. Wang, F.-S. Xiao, *ACS Cent. Sci.* **2020**, *6*, 1685–1697; b) S. M. Csicsery, *Zeolites* **1984**, *4*, 202–213.
- [9] H. Sheng, E. P. Schreiner, W. Zheng, R. F. Lobo, *ChemPhysChem* **2018**, *19*, 504–511.
- [10] D. Gerceker, A. H. Motagamwala, K. R. Rivera-Dones, J. B. Miller, G. W. Huber, M. Mavrikakis, J. A. Dumesic, *ACS Catal.* **2017**, *7*, 2088–2100.
- [11] Y. Xiao, A. Varma, *ACS Catal.* **2018**, *8*, 2735–2740.
- [12] U. Olsbye, S. Svelle, M. Bjørgen, P. Beato, T. V. W. Janssens, F. Joensen, S. Bordiga, K. P. Lillerud, *Angew. Chem. Int. Ed.* **2012**, *51*, 5810–5831.
- [13] a) E. S. Matveenko, M. V. Grigoriev, T. A. Kremleva, E. V. Andrusenko, N. A. Kosinov, *Kinet. Catal.* **2022**, *63*, 351–363; b) N. Kosinov, E. J. M. Hensen, *Adv. Mater.* **2020**, *32*, 2002565.
- [14] J. Z. Chen, Z. Wu, X. Zhang, S. Choi, Y. Xiao, A. Varma, W. Liu, G. Zhang, J. T. Miller, *Catal. Sci. Technol.* **2019**, *9*, 1349–1356.
- [15] G. A. Garcia, L. Nahon, S. Daly, I. Powis, *Nat. Commun.* **2013**, *4*, 2132.
- [16] A. Puente-Urbina, Z. Pan, V. Paunović, P. Šot, P. Hemberger, J. A. van Bokhoven, *Angew. Chem. Int. Ed.* **2021**, *60*, 24002–24007.
- [17] A. Boubnov, H. Lichtenberg, S. Mangold, J.-D. Grunwaldt, *J. Synchrotron Radiat.* **2015**, *22*, 410–426.
- [18] E. J. M. Hensen, Q. Zhu, R. A. J. Janssen, P. C. M. M. Magusin, P. J. Kooyman, R. A. van Santen, *J. Catal.* **2005**, *233*, 123–135.
- [19] P. Marturano, L. Drozdová, G. D. Pirngruber, A. Kogelbauer, R. Prins, *Phys. Chem. Chem. Phys.* **2001**, *3*, 5585–5595.
- [20] N. Kosinov, E. A. Uslamin, L. Meng, A. Parastaei, Y. Liu, E. J. M. Hensen, *Angew. Chem. Int. Ed.* **2019**, *58*, 7068–7072.
- [21] J. L. Weber, I. Dugulan, P. E. de Jongh, K. P. de Jong, *ChemCatChem* **2018**, *10*, 1107–1112.
- [22] X.-W. Liu, S. Zhao, Y. Meng, Q. Peng, A. K. Dearden, C.-F. Huo, Y. Yang, Y.-W. Li, X.-D. Wen, *Sci. Rep.* **2016**, *6*, 26184.
- [23] G. Berlier, G. Spoto, S. Bordiga, G. Ricchiardi, P. Fisicaro, A. Zecchina, I. Rossetti, E. Selli, L. Forni, E. Giamello, C. Lamberti, *J. Catal.* **2002**, *208*, 64–82.

- [24] Q. Wang, J. C. Hanson, A. I. Frenkel, *J. Chem. Phys.* **2008**, 129, 234502.
- [25] J. Krüger, G. A. Garcia, D. Felsmann, K. Moshammer, A. Lackner, A. Brockhinke, L. Nahon, K. Kohse-Höinghaus, *Phys. Chem. Chem. Phys.* **2014**, 16, 22791–22804.
- [26] C. Woywod, W. Domcke, *Chem. Phys.* **1992**, 162, 349–358.
- [27] P. Bruckmann, M. Klessinger, *J. Electron Spectrosc. Relat. Phenom.* **1973**, 2, 341–354.
- [28] D. M. P. Holland, M. A. MacDonald, M. A. Hayes, P. Baltzer, B. Wannberg, M. Lundqvist, L. Karlsson, W. v Niessen, *J. Phys. B* **1996**, 29, 3091–3107.
- [29] P. Carlier, J. E. Dubois, P. Masclet, G. Mouvier, *J. Electron Spectrosc. Relat. Phenom.* **1975**, 7, 55–67.
- [30] Z. Pan, A. Bodí, J. A. van Bokhoven, P. Hemberger, *Phys. Chem. Chem. Phys.* **2022**, 24, 21786–21793.
- [31] a) J. Wang, B. Yang, T. A. Cool, N. Hansen, T. Kasper, *Int. J. Mass Spectrom.* **2008**, 269, 210–220; b) R. A. Mackie, S. W. J. Scully, A. M. Sands, R. Browning, K. F. Dunn, C. J. Latimer, *Int. J. Mass Spectrom.* **2003**, 223–224, 67–79.

Manuscript received: May 3, 2023

Version of record online: July 3, 2023